

Three-dimensional Fold of the Human AQP1 Water Channel Determined at 4 Å Resolution by Electron Crystallography of Two-dimensional Crystals Embedded in Ice

Gang Ren¹, Anchi Cheng¹, Vijay Reddy², Peter Melnyk¹
and Alok K. Mitra^{1*}

¹*Department of Cell Biology and*

²*Department of Molecular Biology, The Scripps Research Institute, 10550 North Torrey Pines Road, La Jolla CA 92037, USA*

Here, we present a three-dimensional (3D) density map of deglycosylated, human erythrocyte aquaporin 1 (AQP1) determined at 4 Å resolution in plane and ~7 Å resolution perpendicular to the bilayer. The map was calculated by analyzing images and electron diffraction patterns recorded from tilted (up to 60°), ice-embedded, frozen-hydrated 2D crystals of AQP1 in lipid bilayer membranes. This map significantly extends the findings related to the folding of the AQP1 polypeptide chain determined by us at a lower, 7 Å by ~20 Å, resolution. The solvent-accessible volume within a monomer has a vestibular architecture, with a narrow, ~6.5 Å diameter constriction near the center of the bilayer, where the location of the water-selective channel is postulated to exist. The clearly resolved densities for the transmembrane helices display the protrusions expected for bulky side-chains. The density in the interior of the helix barrel (putative NPA box region) is better resolved compared to our previous map, suggesting clearer linkage to some of the helices, and it may harbor short stretches of α -helix. At the bilayer extremities, densities for some of the inter-helix hydrophilic loops are visible. Consistent with these observed inter-helix connections, possible models for the threading of the AQP1 polypeptide chain are presented. A preferred model is deduced that agrees with the putative locations of a group of aromatic residues in the amino acid sequence and in the 3D density map.

© 2000 Academic Press

Keywords: aquaporin; membrane-protein structure; two-dimensional crystal; electron crystallography; topology

*Corresponding author

Introduction

The entry and exit of water across the cell membrane is a fundamental physiological process. The observed high level of permeability of water in the case of mammalian erythrocytes and renal proximal tubules led to the discovery of water channels (aquaporins, AQP) (Denker *et al.*, 1988; Smith & Agre, 1991). Aquaporins are members of the MIP (major intrinsic protein) superfamily (Gorin *et al.*, 1984) and are found in both eukaryotes and pro-

karyotes where they serve as channels for rapid dissipation of osmotic gradients across the lipid bilayer (Agre *et al.*, 1995; Verkman *et al.*, 1996). The amino acid sequence of aquaporins displays a tandemly repeating motif, which contains an absolutely conserved Asn-Pro-Ala (NPA) tripeptide sequence. Based on hydrophathy analysis, a topology characterized by six transmembrane segments or more (Wistow *et al.*, 1991) has been suggested.

The abundantly expressed, partially glycosylated, AQP1 (formerly called CHIP28) channel is the archetype in the aquaporin family. It was first discovered in the erythrocyte membranes (Preston & Agre, 1991) and has been the subject of vigorous physiological, biochemical, biophysical and recent structural studies (see, e.g. Heymann *et al.*, 1998;

Abbreviations used: AQP, aquaporin; MIP, major intrinsic protein; DMPC, dimyristoyl phosphatidylcholine; DOPC, dideoyl phosphatidylcholine.

E-mail address of the corresponding author: mitra@scripps.edu

Verkman & Mitra, 2000; Mitra, 2000, for reviews). There is a general consensus that AQP1 selectively transports water and not small chemical species such as H^+ and NH_3 (Zeidel *et al.*, 1992). Recent reports indicate an enhanced level of CO_2 permeability in *Xenopus oocytes* expressing AQP1 (Nakhoul *et al.*, 1998) and in proteoliposomes reconstituted with purified AQP1 (Prasad *et al.*, 1998), however, this is at variance with results obtained by Yang *et al.* (2000). Yool *et al.* (1996) suggested cAMP-dependent water permeability and cation conductance in AQP1-expressing *Xenopus oocytes*. However, subsequently, several researchers failed to duplicate these results (Agre *et al.*, 1997). Biochemical studies of AQP1 purified in Triton X-100 (Smith & Agre, 1991), freeze-fracture studies (Verbavatz *et al.*, 1993) on proteoliposomes reconstituted with AQP1, and CHO cells expressing AQP1, indicated that AQP1 monomers organize as tetramers in the bilayer. On the other hand, several lines of evidence (Preston *et al.*, 1993; Shi *et al.*, 1994; van Hoek *et al.*, 1991; Zhang *et al.*, 1993) show that each monomer is a functional channel. Biochemical studies and immunoelectron microscopy demonstrated that both the N and C termini are located in the cytoplasm (Nielsen *et al.*, 1993; Smith & Agre, 1991; Zeidel *et al.*, 1994). Topology studies at the plasma membrane, using epitope-tagged AQP1, showed that the polypeptide chain threads the bilayer six times (Preston *et al.*, 1994). Jung *et al.* (1994) employed site-directed mutagenesis to show that the amino acid residues neighboring the NPA segments in the first cytoplasmic loop, and the last extra-cellular loop connecting the putative membrane-spanning domains 2, 3 and 5, 6, respectively, are linked to the water transport pathway in AQP1. They envisioned that these hydrophobic loops dip into the bilayer from the two sides and line the water pathway. Here, the transmembrane segments are denoted as 1 to 6 when counted from the N terminus (Figure 1). The passage of water ($\sim 2 \times 10^9$ water molecules/monomer/second (Engel *et al.*, 1994; Zeidel *et al.*, 1994) across the constitutively open pore in AQP1 is blocked by submillimolar concentrations of mercurial reagents. This inhibition has been shown to be due to the binding of mercurials to a single extra cellular cysteine residue, Cys189 (out of four in sequence, Preston *et al.*, 1993) (Figure 1) and is reversed by reducing agents such as β -mercaptoethanol. This result indicates an important functional role for the Cys189.

In order to understand the structural elements that constitute and control the water-selective permeability of AQP1, a detailed knowledge of the high-resolution 3D structure in the bilayer is essential. To this end, 2D crystals of AQP1 have been used to examine the structure using electron crystallography, which has proven to be invaluable for determining high-resolution 3D structures of membrane proteins (Grigorieff *et al.*, 1996; Henderson *et al.*, 1990; Kimura *et al.*, 1997; Kühlbrandt *et al.*, 1994). Projection maps of AQP1

were determined by electron cryo-crystallography by three groups of workers (Jap & Li, 1995; Mitra *et al.*, 1995; Walz *et al.*, 1995). These analyses differed in the source and level of glycosylation of the protein, conditions used for 2D crystallization and specimen cryo-preservation. Walz *et al.* (1995) used glucose-embedded native, partially glycosylated AQP1 from human erythrocytes that were crystallized in lipids extracted from *Escherichia coli*. Glucose embedding was also employed by Jap & Li (1995), who used native bovine AQP1 crystallized in dimyristoyl phosphatidylcholine (DMPC). We (Mitra *et al.*, 1995) crystallized deglycosylated, human erythrocyte AQP1 in dioleoyl phosphatidylcholine (DOPC) bilayers and examined the frozen-hydrated crystals preserved in vitrified buffer. Notwithstanding the differences stated above, the three projection maps revealed overall similarities, characterized by tetrameric packing of the AQP1 monomers and multiple density peaks in each monomer, suggestive of α -helices. Subsequently, a 7 Å resolution, 3D density map of AQP1 was determined (Cheng *et al.*, 1997) from an analysis of minimal dose images and electron-diffraction patterns recorded from ice-embedded 2D crystals. Three-dimensional density maps, at a similar level of resolution were reported by the other two groups (Li *et al.*, 1997; Walz *et al.*, 1997), which were determined using specimens preserved in trehalose; the tilted projections comprised of images and electron diffraction patterns (Walz *et al.*, 1997) and only images (Li *et al.*, 1997). All three maps reveal a barrel formed by six helices surrounding additional density; the helices pack with a right-handed twist in the models of Cheng *et al.* (1997) and Walz *et al.* (1997) but with a left-handed twist in the model of Li *et al.* (1997). Engel and colleagues (Walz *et al.* 1997) provided a possible assignment of the six helices to the polypeptide sequence based on the observed features of the 3D density map (Walz *et al.*, 1997) and their results from atomic force microscopy (AFM) studies (Walz *et al.*, 1996). However, recently this group (Heymann & Engel, 2000) suggested a different assignment, based on amino acid sequence analysis of aquaporins.

We present an improved 3D density map of AQP1, which was generated by including data up to 4 Å resolution recorded from electron diffraction patterns and images of 2D crystals tilted up to 60°. In the density map, the clearly resolved densities for the transmembrane helices display protrusions expected for bulky side-chains. The density in the interior of the helix barrel (putative NPA box region) is better resolved and suggests clearer linkage to some of the helices. Densities for some of the inter-helix hydrophilic loops in a monomer are now visible at the bilayer extremities. Unambiguous assignment of individual side-chains in the density proved to be difficult because of limited vertical resolution (~ 7 Å). However, consistent with deductions from the improved map, we present models for the threading of the AQP1 poly-

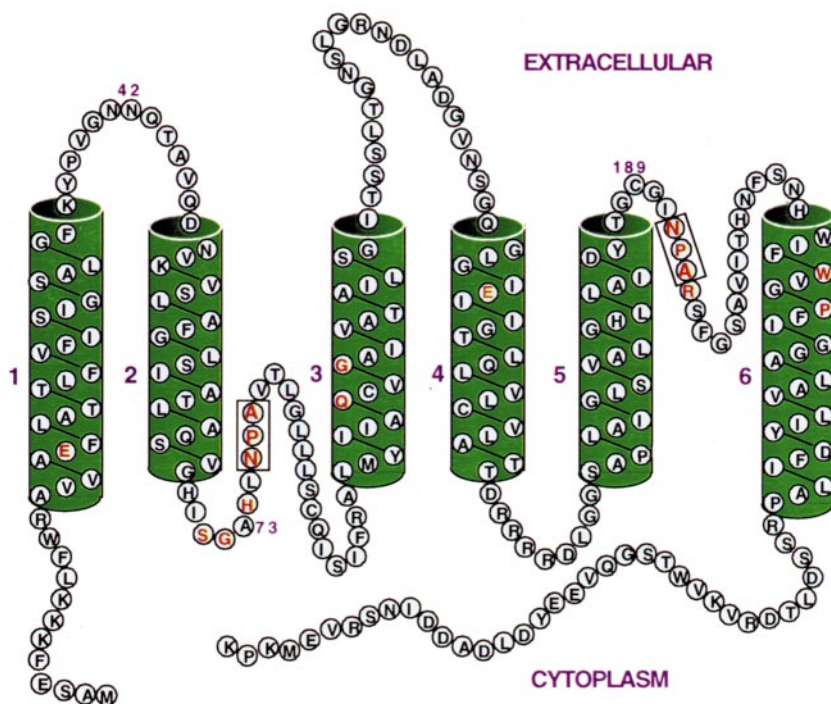


Figure 1. A display of the polypeptide sequence of human AQP1 indicating the six primary transmembrane segments which were deduced using a consensus secondary-structure prediction algorithm (X. Hu and K. Schulten, personal communication). The exact boundary between the lipid-embedded and the solution-facing regions is ill defined. Indicated are Cys189, the mercury-sensitive site and the analogous Ala73; Asn42, the site of glycosylation; the conserved NPA boxes; and some of the other residues conserved among mammalian aquaporins.

peptide chain and suggest testable hypotheses concerning the biological function of AQP1 as it relates to the polypeptide sequence. One of the proposed topology models, identified as the preferred model, agrees with the putative locations of a group of aromatic residues in the amino acid sequence and in the 3D density map.

Results

Crystallographic data

The statistics of the 3D data, which extends to a resolution of 4.0 Å, are summarized in Table 1. Computed Fourier transform of a selected high-tilt image (55°) and electron diffraction patterns from a nominally untilted and a highly tilted (55°) 2D crystal are shown in Figures 2 and 3, respectively. The cumulative distribution of data for all the images and diffraction patterns, which were included in determining the variation of the transform along various lattice lines, is shown in Figure 5.

Description of the 3D map

Packing of the α -helices

The 3D density of an AQP1 monomer viewed approximately perpendicular to the membrane plane is shown in Figure 6. As observed in ~6-7 Å resolution maps (Walz *et al.*, 1997; Li *et al.*, 1997; Cheng *et al.*, 1997), a barrel of six significantly tilted α -helices (A to F), each sufficient in length (~36-44 Å) to span the bilayer are arranged with a right-handed twist. This helix barrel characterizing

the core structure of the monomer, encloses a central density (Figure 6 and see below) that has been attributed to the NPA box regions (Walz *et al.*, 1997; Li *et al.*, 1997; Cheng *et al.*, 1997).

Even though pairs of α -helices can pack with either a left or right-handed twist (Chothia *et al.*, 1981), α -helix bundles usually display a left-handed twist in protein structures. The helix barrel in the AQP1 monomer display a right-handed twist; however, the bundle comprising of helices B, C of one monomer and D, E of an adjacent monomer is packed at the monomer interface with a more conventional left-handed twist. Examples of right-handed packing in α -helix barrels, as in the case of AQP1, are in the 3D structures of rat liver dihydropteridine (Varughese *et al.*, 1992) and in the nucleosome core particle (Luger *et al.*, 1997). The small-size amino acid residues Gly and Ala, which are quite abundant, especially in segments 2, 3, 5 and 6 (Figure 1), may encourage the tight packing that separate the six helices in the monomer into three pairs A-B, C-D and E-F.

Consistent with the improved resolution of the map, densities for the α -helical segments (some more than others) display discernible protrusions (more than twice the standard deviation of the map density) along their length. Figure 7 shows the excised density for helix A to indicate, as an example, the surface features revealed in the improved density map, and demonstrates the helical periodicity of the observed protrusions, allowing the positioning of C α backbone in a helical configuration in the density. These surface features were absent or less apparent in the earlier lower-resolution map, and could represent the locations

Table 1. Electron crystallographic data

Two-side plane group	$p42_12$
Unit cell dimension (Å)	$a=b=99.58(\pm 0.50)$ Å, $c=100$
IQ cut-off ^a of data	≤ 7
Number of amplitudes measured	36,019
Number of phases measured	16,129
Number of structure factors used in map calculation ^b	2441
Completeness (%)	(100-14 Å) 93 (14-6 Å) 82 (6-4.5 Å) 59 (4.5-4 Å) 37 (100-4 Å) 60
Overall	
In-plane resolution (Å)	4
Estimated resolution normal (Å) to the bilayer ^c	7
Electron diffraction	
Resolution limit (Å)	3.7
Maximum tilt (deg.)	57.5
Number of patterns by tilt angle (deg.)	0-15 (14) 15-40 (19) 40-60 (11) Total: 44
Number of merged intensities	36,019
R_{Friedel} ^d (%)	6.3-21.8 (average=12.9)
R_{merge} ^e (%)	15.2-40.8 (average=27.9)
Image	
Resolution limit (Å)	4.0
Maximum tilt (deg.)	60.2
Number of images by tilt angle (deg.)	0-15 (20) 15-25 (10) 25-40 (13) 40-50 (15) 50-60 (14) Total: 72
Resolution zones (Å), number of measurements and phase residual ^f (deg.)	(100-14) 3896, 17.3 (14-6) 12 564, 19.6 (6-4.5) 6273, 31.4 (4.5-4) 1781, 42.2 (100-4) 25 328, 21.0
Overall	

^a Nomenclature by Henderson *et al.* (1986)

^b With figure of merit ≥ 0.27 out of a total of 4322.

^c Based on calculation of point-spread function (Unger *et al.*, 1995).

^d $R_{\text{Friedel}} = \sum_{hk} |I_{hk} - I_{\bar{h}\bar{k}}| / \sum_{hk} (I_{hk} + I_{\bar{h}\bar{k}})$.

^e $R_{\text{merge}} = \sum_{hk} |I_{\text{obs}} - I_{\text{fit}}| / \sum_{hk} I_{\text{fit}}$.

^f Weighting based on amplitudes.

of bulky side-chains revealed in the higher resolution map, as shown in Figure 7. The region near the four-fold axis at the interface of the four monomers appears to lack significant protein density (Figure 6); however, its diameter is smaller than that seen before (Cheng *et al.*, 1997) because of the appearance of protrusions on density for helices C and D. All of the helices show some degree of curvature, especially helix D and helix F. These bends in the helices could be due to the presence of a number of glycine and/or proline residues located within the putative membrane-spanning regions of the polypeptide chain (Figure 1) and/or due to a π -bulge, as seen in bacteriorhodopsin structure (Luecke *et al.*, 1999). On the proximal side (as viewed in Figure 6), intra-monomer, inter-helix contacts possibly mediated by side-chains are seen between helices A and B, between helices C and D, between helices E and F and near the middle of the monomer between helices B and C and helices E and F.

Pseudo 2-fold symmetry

We carried out a careful analysis of the current, higher-resolution density map to scrutinize the presence of an in-plane pseudo 2-fold axis of symmetry within the hydrophobic core of the molecule we had previously discovered (Cheng *et al.*, 1997) and also suggested by Li *et al.* (1997). For this purpose, a cross-correlation calculation (see Materials and Methods) was pursued using the density attributed to a monomer, with the boundary for a monomer identified based on our previous 3D density map (Cheng *et al.*, 1997). This analysis showed that the presence of in-plane pseudo 2-fold axis of symmetry, which approximately bisects the helix pairs C, D and A, F and passes through the central density is strongly revealed only when data up to 6 Å resolution were used (Figure 8). However, the signal was not significant when 3D data to the highest resolution were included (data not shown). This result indicates that the local symmetry is

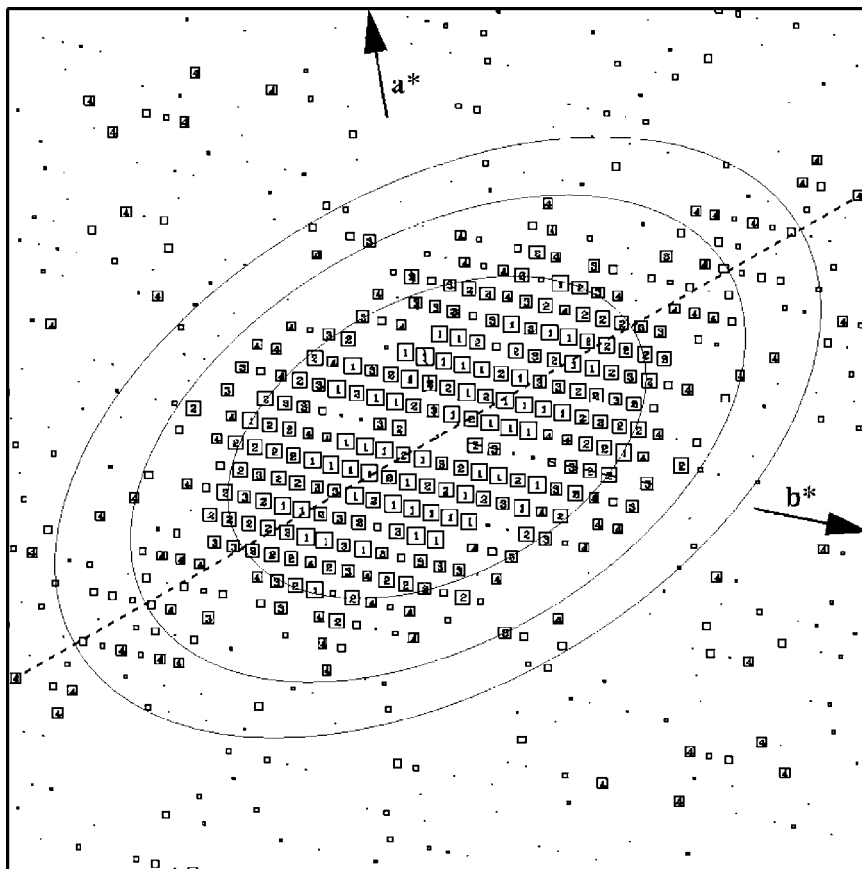


Figure 2. Computed transform of an image of a 55° tilted crystal after correcting for the effects of lattice distortion and defocus. The ellipses are drawn at 3D resolution of 7 Å, 5 Å and 4 Å. Spots up to $IQ = 7$ (Henderson *et al.*, 1986) are indicated, with those between $IQ = 1$ and 4 marked by the IQ value.

strong only when features such as the spatial locations, and presumably the backbones of the α -helical segments of the two halves of the polypeptide chain (Mitsuoka *et al.*, 1999) are compared. Alternatively, the location of the helices belonging to the tandemly repeating motifs are indeed constrained by the pseudo symmetry, but the symmetry is obscured at higher resolution due to non-identity of the side-chain composition and exact helix orientation. Intra-molecular pseudo 2-fold symmetry has been noted in the structure of LHC-II (Kühlbrandt & Wang, 1991; Kühlbrandt *et al.*, 1994) where the symmetry axis, oriented perpendicular to the membrane plane, is located between two helices showing sequence homology. This has also been noted in the structure of the soluble protein β -lactamase from *Bacillus cereus* (Carfi *et al.*, 1995) where it relates two polypeptide domains, indicating a possible gene duplication.

Protein density in addition to those attributed to the transmembrane helices

Strong bands of density, some of which are continuous and comparable in strength to that for the transmembrane helices, can be identified at the extremities of some of the helices. These segments of density are located either at the extralayer sur-

faces or are disposed within the helix barrel defining the putative NPA box region, and suggest the locations of some of the ordered inter-helical loops. Our observations related to the various putative linkages displayed in the 3D density map and illustrated individually in Figure 9 are discussed below. "Proximal" and "distal" refer to the near and away faces, respectively with regards to the density map shown in Figure 6.

(1) Density within the helix barrel (Figure 9a). The density within the helix barrel appears as two V-shaped segments arranged tip-to-tip, similar to that seen by Mitsuoka *et al.* (1999). This density attributed to the NPA box regions and located in front of the lipid-facing helices A and F is better resolved than in our earlier map.

(2) Proximal edge of helix F to the central density (Figure 9(b)). This linkage is revealed as an almost continuous segment of density, separated from the extremity of any other helix. Near the middle of the bilayer the density broadens to a dimension comparable to that of a transmembrane α -helix and may harbor a short segment in α -helical conformation. Mitsuoka *et al.* (1999) has calculated at a (4.5 Å) resolution, that this relatively wider portion of the linkage represents a short α -helix.

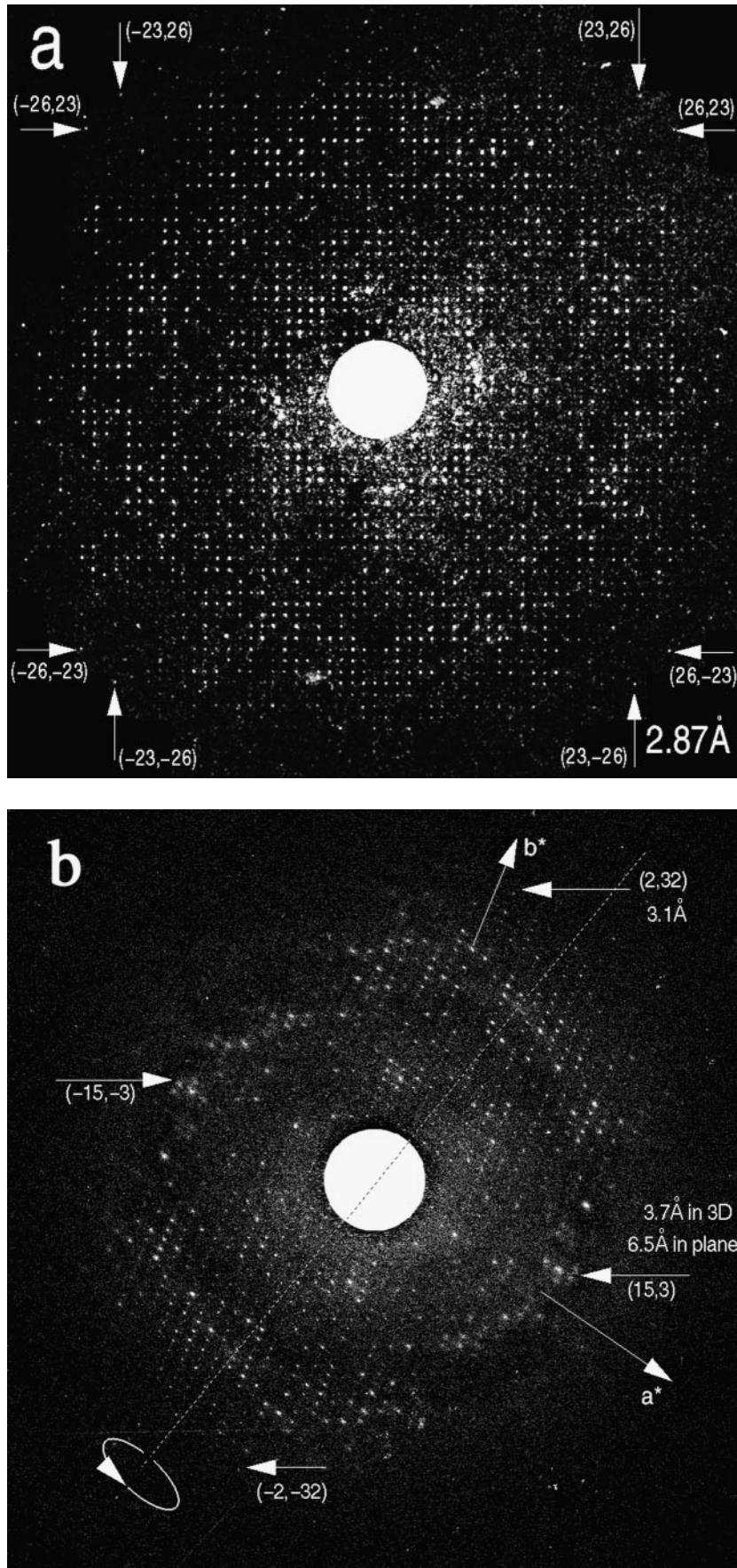


Figure 3. Background-subtracted displays of electron diffraction patterns recorded from a nominally untilted (a) and a nominally 55° -tilted 2D crystal (b). (b) The position of the tilt axis and a few high-resolution reflections are marked.

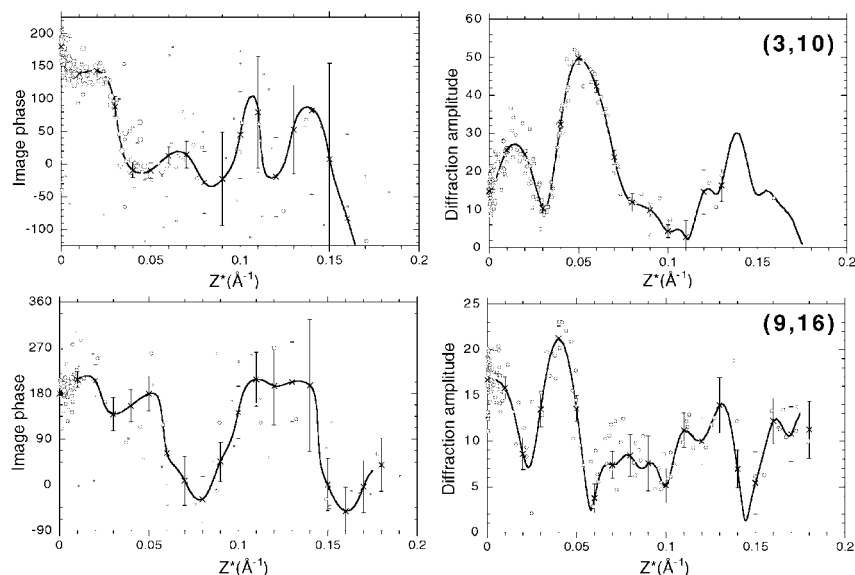


Figure 4. Amplitude and phase profiles for two representative lattice lines determined by using the program LAT-LINE (Agard, 1983). Open circles represent observed data and x represent sampled values. In the phase profiles larger circles represent measurements with lower IQ values and the vertical bars at the sampled positions equal twice the estimated errors used in the figure of merit calculation.

(3) Proximal edge of helix D to the central density (Figure 9(c)). As in observation (2) above, this linkage is separated from the extremity of any other helix, is of similar strength as it dips towards the middle of bilayer from the proximal end of helix D. This linkage and that noted in (2) outlines the wall of the proposed water-selective pore near the bilayer center (see below).

(4) Distal edge of helix F to the central density (Figure 9(d)). This connection is again isolated away from the extremity of any other helix, is mostly continuous and was only partly visible in our earlier 7 Å map.

(5) Distal edge of helix A to the central density (Figure 9(e)). This continuous linkage also widens near the middle of the bilayer as in the case of

observation (2), but is somewhat narrower than (2) throughout its extent. The relatively wider portion of this density may harbor a short α -helix as has again been suggested also by Mitsuoka *et al.* (1999).

(6) Density between proximal extremities of helices B and C (Figure 9(f)). The only visible linkage (see also Figure 6) between adjacent helices on the proximal face is a relatively short connection between B and C. Although this bridging density curves towards to the edge of helix D of the adjacent monomer it clearly extends to contact the top of helix C in the same monomer.

(7) Density at the distal edges of helices D and E (Figure 9(g)). There is an assembly of somewhat disconnected peaks of density at this region neigh-

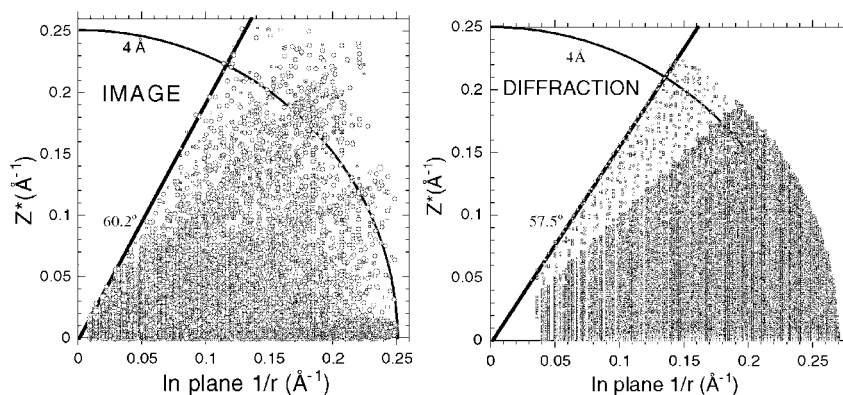


Figure 5. (a) The distribution of all significant measurements extracted from the images. The sector delineates the maximum tilt. (b) Distribution of measured data (amplitudes) calculated from electron diffraction patterns recorded from tilted crystals. The sector delineates maximum tilt.

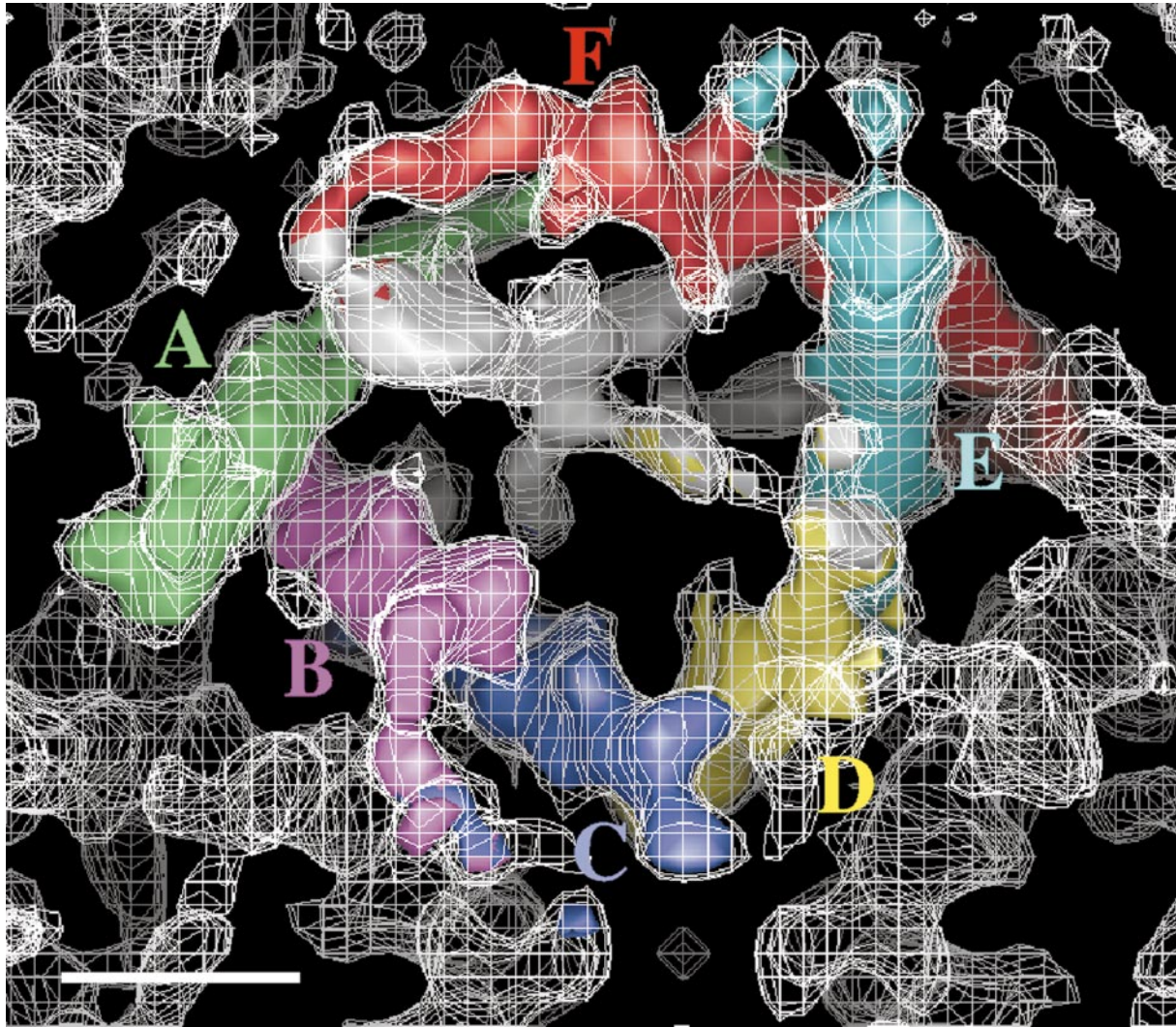


Figure 6. Three-dimensional density map of ice-embedded, frozen-hydrated AQP1 at in-plane resolution of 4 Å and at a resolution of ~ 7 Å normal to the bilayer (see the text for resolution calculation). One monomer with the densities for the tilted transmembrane α -helices (A-F) and portions of adjacent monomers are shown. The chicken-wire density is at 1.5σ , while the solid density is at 2σ of the mean density of the map. The density enclosed by the helix barrel and located near the middle of the bilayer (white) is attributed to the NPA box region of the polypeptide chain. This Figure and Figures 9, 10, 11 and 12 were generated using the AVS software (Upson *et al.*, 1989). The same color code for the transmembrane helices are followed throughout, except in Figure 7. The scale bar represents 10 Å.

boring the crystallographic 4-fold axis of symmetry. Based on the assigned monomer boundary, the logical interpretation of this feature is that it represents a bridge between the ends of helices D and E that also interacts with the distal edge of helix C of an adjacent monomer.

(8) Densities at the distal edges of helices B and C (Figure 9(h)). A collection of density peaks is located in the space between the middle of the bilayer and the distal edge of helices B and C. These peaks show apparent connection to the central density, but no clear interpretation can be made, even when the map is rendered at less than one standard deviation contour level. Because of limited available volume in this region, our working hypothesis is that the density primarily rep-

resents bridge between either B or C to the central density.

Discussion

This work and the recent 4.6 Å resolution analysis of acetyl-choline receptor reported by Unwin & colleagues (Miyazawa *et al.*, 1999) represent the near-atomic resolution 3D structural analyses of ice-embedded specimens determined by electron cryo-crystallography. This is noteworthy in view of the fact that, to date, structural studies to derive atomic or near-atomic resolution structure by electron crystallography have been exclusively carried



Figure 7. Excised density of helix A with a poly-alanine chain modeled into the density. The density was rotated so that the helix axis is approximately normal to the viewing direction. Protrusions that may be attributed to bulky side-chains are clearly visible. As shown, two tryptophan residues and a phenylalanine residue were positioned according to the preferred polypeptide threading model (Figure 11 below) and at locations corresponding to those in the extracellular face of the C-terminal helix 6 (Figure 1). Map is rendered at 1σ of the mean density and the Figure was generated using the program O.

out on specimens preserved in sugars such as tannic acid (Kühlbrandt *et al.*, 1994), trehalose (Kimura *et al.*, 1997; Nogales *et al.*, 1998) or glucose (Grigorieff *et al.*, 1996). Our ability to record high-tilt, high-resolution electron diffraction patterns (Figure 3(b)) using ice-embedded specimens shows that acquisition of isotropic 3D data to near-atomic resolution (~ 3.7 Å) from such specimens is feasible. Also, at a comparable resolution, the statistics, based on R_{merge} and R_{friedel} values given in Table 1, compare very favorably with those for LHC-II (Kühlbrandt and Wang, 1991) but are somewhat poorer than those for bacteriorhodopsin (Baldwin & Henderson, 1984; Ceska & Henderson, 1990) for

which data were acquired from crystals sustained in sugar.

During the process of 3D merging of electron crystallographic data, it was noticed that data from a set of good, high-resolution images and a set of good, high-resolution electron diffraction patterns failed to agree with other merged images and diffraction patterns, respectively. The phases from such images (of which 16 were at $>45^\circ$ tilt) consistently yielded high (typically $>30^\circ$) residual even at low (~ 14 Å) resolution and the sets of intensities from such diffraction patterns showed R_{merge} values that were more than twice the average value. In all, 28 good images and 17 good diffraction patterns were discarded. It is likely that these images and diffraction patterns were from crystals harboring an alternate packing scheme for AQP1 as described recently (Ren *et al.*, 2000). In the computed transforms of our best images recorded from highly tilted crystals, the distribution of significant spots clearly showed anisotropy in achievable 3D resolution (Figure 2). Thus, the resolution perpendicular to tilt axis was weak beyond ~ 5 Å, whereas the resolution parallel to tilt axis reached ~ 4 Å. This, therefore, limited the vertical resolution in our 3D density map. On the other hand, nominally untilted crystals frequently yielded images containing reproducible, isotropic data to beyond 3.7 Å resolution (data not shown; Ren *et al.*, 2000). Specimen charging has been considered to be a significant contributing factor in this anisotropy and loss of resolution during electron cryomicroscopy. Brink *et al.* (1998a) analyzed this problem and suggested a physical model for “resolution-degrading” effects. In this model, during the image recording, the Coulombic interaction between the primary electrons and the secondary Auger electrons causes movements of the specimen, which assume varying directions when the specimen is tilted. Coupled with lack of specimen flatness, the cumulative effect is the blurring of spots, especially those perpendicular to the tilt axis (Figure 2). We found that sandwiching the crystals between two layers of carbon produced the best tilted images, presumably by improving the electrical conductivity of vitrified specimens (Rader & Lamvik, 1992; Brink *et al.*, 1998b); however, the image contrast is still poorer than that expected based on the recorded electron diffraction patterns (Figure 3).

Model for the AQP1 topology

Because of the limited vertical resolution of our 3D map, unambiguous registration of the primary sequence into the density proved to be difficult. In order to arrive at rational model(s) for the threading of the polypeptide chain (topology) we exploited the presence of observed linkages in the 3D density map discussed above, employed the so-called “hourglass” arrangement in which the NPA containing inter-helix loops fold into the bilayer (Jung *et al.*, 1994), and considered clues from pro-

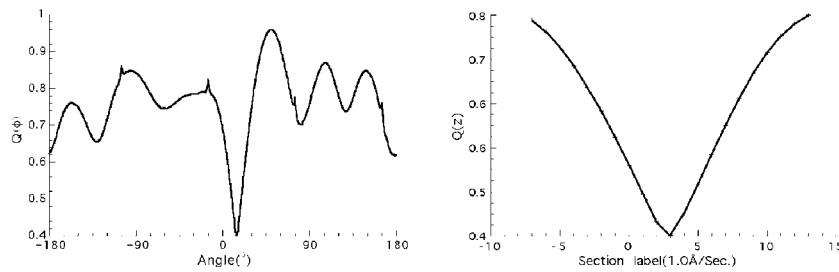


Figure 8. Results of cross-correlation calculations based on 3D data up to 6 Å resolution to identify (a) the orientation (ϕ) of the pseudo 2-fold axis with respect to a lattice edge and (b) its position along the z-axis (see Materials and Methods for details).

tease sensitivity, amino acid sequence and mutagenesis experiments. Below, we have considered both possible orientations for a given AQP1 monomer in the 3D density map under class 1 (proximal face of density map in Figure 6 cytoplasmic) and class 2 (distal face of density map in Figure 6 cytoplasmic) models.

Clues from protease sensitivity, amino acid sequence and mutagenesis experiments

(1) Susceptibility of AQP1 to limited proteolysis has indicated that only the long (~4 kDa) C terminus is readily cleaved, based on experiments on red blood cell inside out vesicles enriched in AQP1 (Zeidel *et al.*, 1994). We see (data not shown) a similar cleavage pattern in the case of AQP1 2D crystals (also noted by Walz *et al.*, 1996) and for solubilized AQP1 in OG. These results suggest that within the extrabilayer mass it is primarily the interhelical loops that are likely to be structurally rigid and/or apposed close to the bilayer surface.

(2) The long NPA-containing loops (5-6 and 2-3 inter-helix linkers) in the MIP family show a strong level of sequence homology (Pao *et al.*, 1991) and display significant signals in hydrophathy plots (Wistow *et al.*, 1991). Residues in these loops have been shown (Jung *et al.*, 1994) and predicted to be functionally important (Froger *et al.*, 1998). It is reasonable to assume that these loops are well ordered in the 3D structure and therefore are expected to appear with strong density in the 3D map.

(3) Helices 4 and 5 are likely to be adjacent in space because of the short cytoplasmic linker, which is a feature in the aquaporin family. This is also likely to be the case for helices 1 and 2, and we note that this extracellular loop is particularly short in the highly homologous renal collecting duct aquaporin AQP2 (Deen *et al.*, 1994).

(4) A functional role for the 3-4 linker in water transport in AQP2 has been suggested from mutagenesis experiments by Bai *et al.* (1996). The 3-4 inter-helix loop may also be involved in influencing solute selectivity in glycerol transporters where this linker is significantly longer (Froger *et al.*, 1998). It is likely, therefore, that this loop, or

at least a portion of it, is sequestered in the interior of the helix barrel proximal to the solute pathway.

Class 1

The only strong linkage observed in the proximal side is the helix F to D connection *via* the central density (attributed to the NPA region) (Figure 9(b) and (c)). The logical choice for the F to D linkage is the 2-3 NPA loop and considering point (2) above and Figure 9(g), the assignment of helix F = helix 3, helix D = helix 2 and helix E = N-terminal helix 1 follows. Observation of Figure 9(f) and (h) and point (3) above leads to the assignment of helix B = helix 4 or 5 and helix C = helix 5 or 4. This leaves helix A as the C-terminal helix 6. The two possible models are then (1) A = 6, B = 5, C = 4, D = 2, E = 1 and F = 3 and (2) A = 6, B = 4, C = 5, D = 2, E = 1 and F = 3. Consistent with Figure 9(e) and (h), the 5-6 linker on the distal side is then either helix A to helix C or helix B *via* the central density. The 3-4 linker is ascribed to the distal connection between helix F and helix B, with part of the bridging density disposed within the interior of the helix barrel. Such an arrangement of this linker is consistent with point (4) above. No significant density is seen at the proximal end of helix A (helix 6), consistent with the C-terminal tail being disordered (point (1) above).

Class 2

The choice for the F to D linkage is the 5-6 NPA loop and considering Figure 9(g) and point (2) above, the assignment helix F = helix 6, helix D = helix 5 and helix E = helix 4 is reached for one half of the sequence. Again, observing Figure 9(f) and (h) and point (3) above leads to the assignment of helix B = helix 1 or 2 and helix C = helix 2 or 1. The assignment of helix A is then helix 3. The 2 possible models are then: (1) A = 3, B = 2, C = 1, D = 5, E = 4 and F = 6 and (2) A = 3, B = 1, C = 2, D = 5, E = 4 and F = 6. Consistent with Figure 9(e) and (h), the 2-3 linker on the distal side is then helix A to helix C or helix B *via* the central density. It is to be noted that density for the 3-4 linker in the location implied in this class of model, i.e.

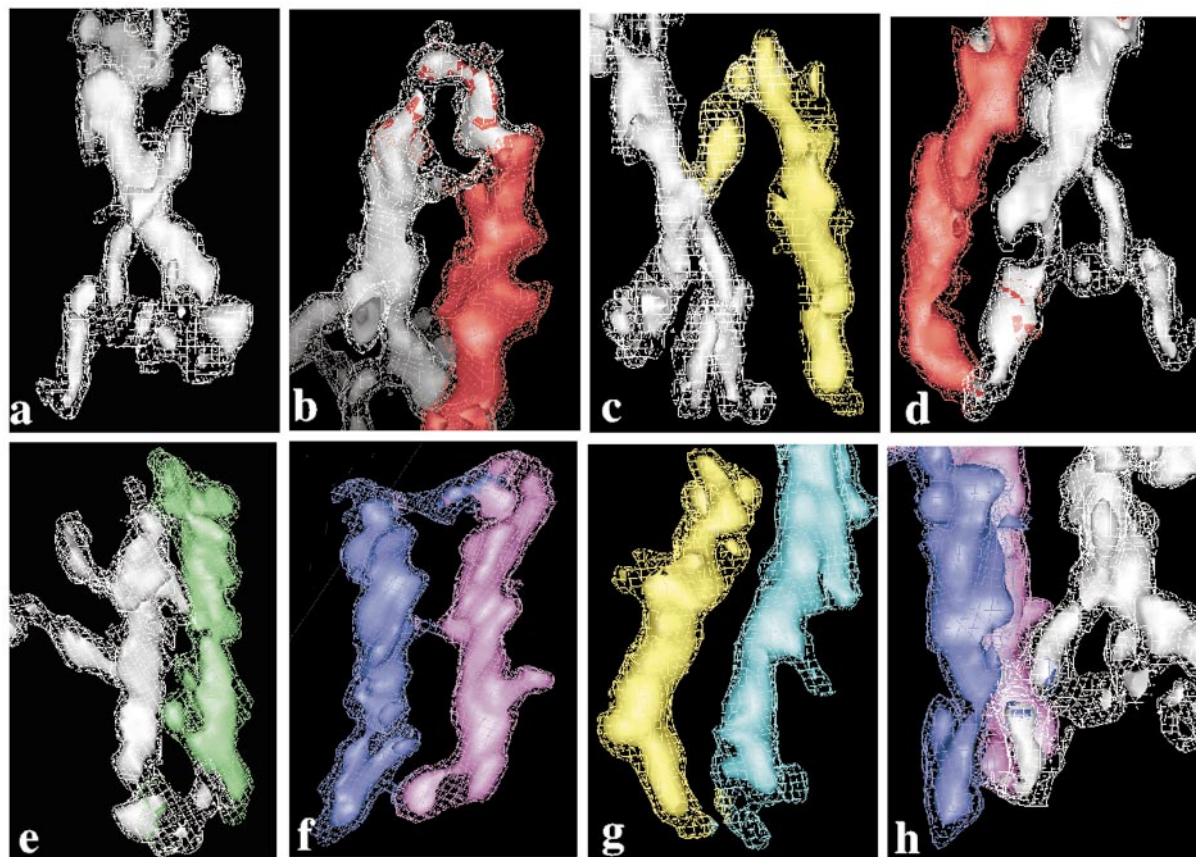


Figure 9. Densities at the extremities of some of the six transmembrane helices and within the interior of a monomer. The top and bottom of each Figure correspond to the proximal and distal edges of Figure 6, respectively. (a) Density within the helix barrel attributed to the putative NPA box regions. (b) Proximal edge of helix F to the central density. (c) Proximal edge of helix D to the central density. (d) Distal edge of helix F to the central density. (e) Distal edge of helix A to the central density, (f) Density between proximal extremities of helices B and C. (g) Density at the distal edges of helices D and E. (h) Densities at the distal edges of helices B and C.

proximal edges of helices A and E, is not apparent in the 3D map.

Figure 10(a) and (b) show the arrangements of the six helices in the monomer density according to the two classes of proposed topology models. Since density corresponding, at least in part, to all of the inter-helix linkers can be ascribed to density features in the 3D map, class 1 models are clearly favored, and model 2 of this class is shown in the form of helical ribbon drawing in Figure 11. This polypeptide-threading scheme agrees with the putative locations of a group of aromatic residues modeled in helix A (=helix 6) (Figure 7) and their positions in the amino acid sequence at the extracellular face of the C-terminal helix. The topological location of helix 5 in this preferred model is also consistent with the location of the extracellular Cys189 in projection indicated from a Fourier difference map calculated from analysis of electron diffraction data from 2D crystals of AQP1 incubated with pCMBS (Ren *et al.*, unpublished result). On the other hand, class 2 models agree with the proposal by Walz *et al.* (1996) that the side of the AQP1 molecule with larger mass faces the cyto-

plasm, based on their surface relief reconstruction from unidirectionally metal shadowed AQP1 2D crystals, which were digested with carboxypeptidase Y.

All the four proposed models require the presence of a "cross over" 3-4 linkage. The irregular arrangement of helices in the proposed polypeptide-threading schemes is not incompatible with membrane topogenesis. This is because the insertion process *in vivo* proceeds with the sequential threading of helix pairs (see review by Bibi, 1998 and papers cited therein) and the 3-4 linker is of sufficient length to allow possible rearrangement of the helices in the plane of the bilayer. It is also noted, for example, that in the X-ray crystal structure of subunit III of cytochrome *c* oxidase from *Paracoccus denitrificans*, an irregular arrangement of seven transmembrane α -helices has been observed (Iwata *et al.*, 1996).

Although the current models are derived based only on the observed connections in the higher 4 Å resolution 3D density map, it is interesting that one of the models in both cases (the second model) implies the existence of 2-fold symmetry, although

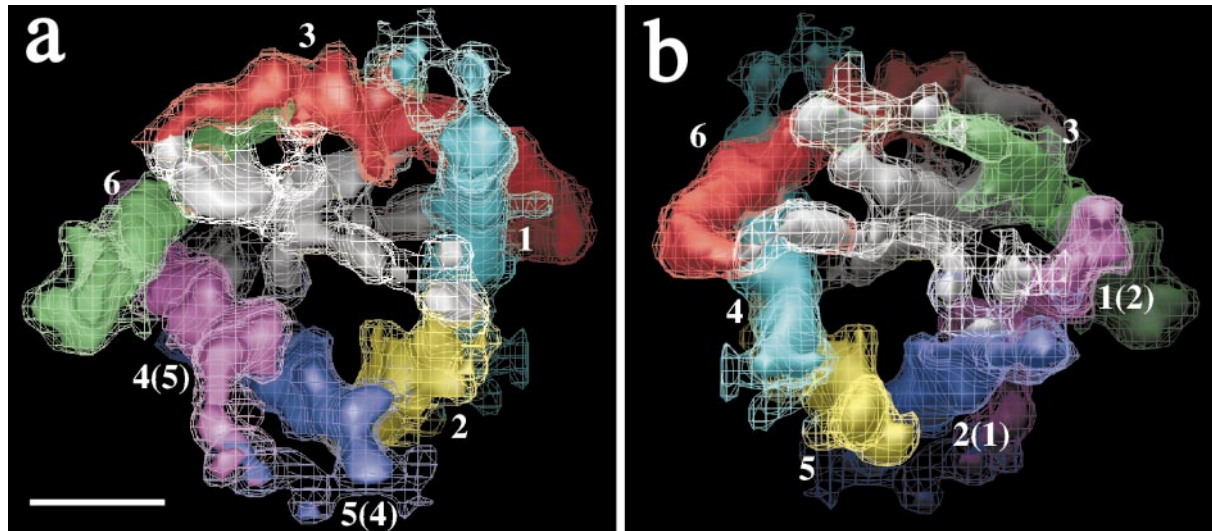


Figure 10. Proposed threading models for the AQP1 polypeptide chain based on deductions from the 4 Å 3D density map, information from the polypeptide sequence and clues from mutagenesis and biochemical studies (see the text). (a) Class 1, corresponding to the proximal face of density map in Figure 6 cytoplasmic. The scale bar represents 10 Å. (b) Class 2, corresponding to the distal face of density map in Figure 6 cytoplasmic. The viewing direction (normal to the bilayer) for the excised density of an AQP1 monomer in (a) is the same as in Figure 6 while it is the opposite in (b).

no assumptions of symmetry were applied in the derivation. We had argued (Cheng *et al.*, 1997) that strict imposition of the in-plane pseudo 2-fold symmetry is consistent with only a handful of topology models, and one such model reported by Verkman & Mitra (2000) is identical to model 2 of class 2. Recently, based on analyses of the periodicity of sequence conservation and hydrophobicity in the polypeptide sequences of aquaporins, Heymann &

Engel (2000) have provided a topology model for AQP1 that is valid for both orientations. This model implies an in-plane pseudo 2-fold symmetry but is different from that proposed earlier (Heymann *et al.*, 1998) which ascribed a sidedness to the AQP1 monomer in their 3D density map (Walz *et al.*, 1997). We note that our preferred model agrees with the oppositely-oriented counterpart of the model presented by Heymann & Engel

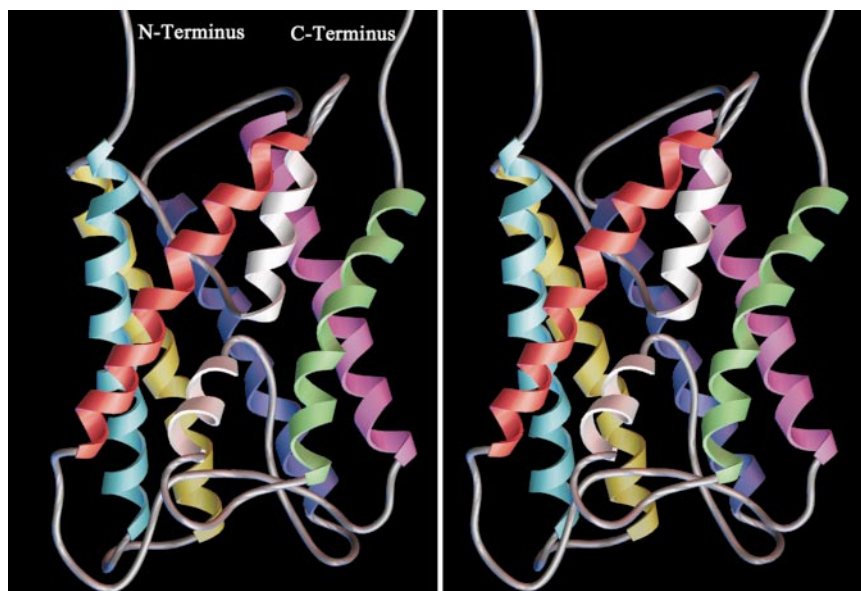


Figure 11. Helical ribbon representation of AQP1 topology corresponding to the preferred class 1 model. The monomer is viewed parallel to the 4-fold axis with the lipid-embedded face proximal. Apart from the six transmembrane α -helices, two short putative α -helices (in white), one in the cytoplasmic NPA-containing loop (see text and Figure 9(b)), and the other in the extracellular NPA-containing loop (see the text and Figure 9(e)) are also shown. The paths of the non-helical regions in the inter-helix linker, which were positioned to match the observed density, are approximate.

(2000) and disagree with AFM results (Walz *et al.*, 1996). Notwithstanding the agreements, the validity of the topology can only be established when either ancillary information regarding the relative locations of marker residues, obtained for example from biophysical/mutagenesis approaches, are available or when the atomic resolution structure is solved.

Interactions stabilizing the AQP1 quaternary structure

Whereas the outside surfaces of helices A and F delineate the membrane-embedded face of the molecule (noted also by Li *et al.* (1997)) those for the other four-helices (B, C, D and E) define a buried surface at the interface between the monomers. Interactions stabilizing the quaternary organization are likely to be elaborated in this buried surface. As noted (above and in Cheng *et al.* (1997)) helices B, C of one monomer and D, E of adjacent monomer display intimate packing and the following details of the interaction are revealed. The loop between helices B and C appears to interact with the end of helix D of an adjacent monomer (Figure 9(g)), the distal edges of helices D and E interact with the distal edge of helix C of an adjacent monomer and around the 4-fold axis helices C and D of adjacent monomers are in close apposition suggesting stabilizing interactions.

Location and architecture of the channel

All published lines of evidence (Preston *et al.*, 1993; Shi *et al.*, 1994; van Hoek *et al.*, 1991; Zhang *et al.*, 1993) indicate that the AQP1 monomer contains the functional channel. The smoothed, surface-rendered volume of low density (negative density) representing the solvent-accessible region enclosed by the helix barrel shown in Figure 12 has a vestibular shape (Mitra *et al.*, 1995; Cheng *et al.*, 1997). This volume is relatively wide on both faces of the molecule but narrows down to a diameter of ~ 6.5 Å near the center. This narrow region located in the hydrophobic core of the molecule may represent the physical constriction defining the selectivity filter. The vestibular region is bound by the tightly-packed helices C and D near the 4-fold axis, and by the wall of density within the barrel attributed to the NPA boxes (Figure 9(b)), thereby ensuring entry and exit to the narrow constriction only from the top and bottom of the monomer. Because the demarcation of protein and solvent regions is somewhat arbitrary, and the fact that the side-chains have not been positioned due to limited vertical resolution of the map may mean that the actual diameter of the constriction is smaller. The side-chains that define the narrow constriction may include residues contributed by helices C and D which display bumps pointing to the putative pore region (Figure 6) and based on the proposed threading models (Figure 10(a) and (b)) the helices 1, 2, 4 and 5 that are proximal to the

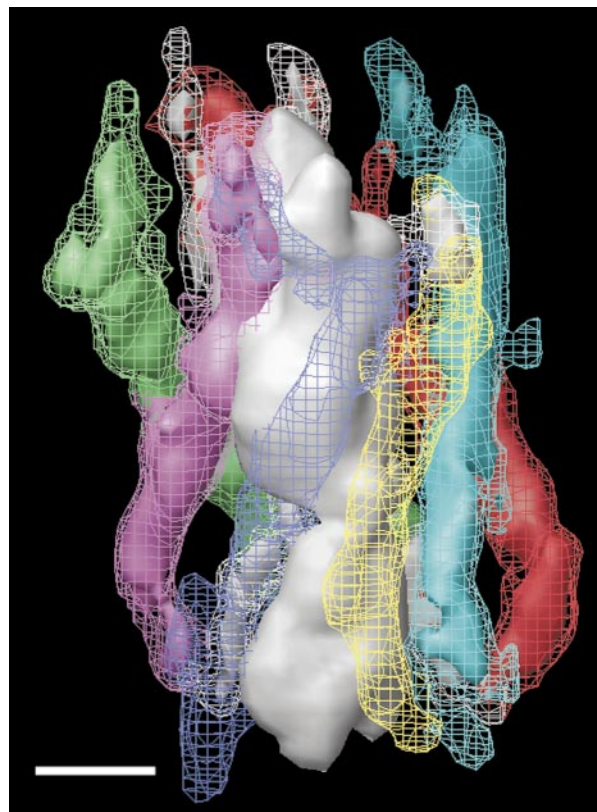


Figure 12. The solvent-accessible region represented as light gray, volume enclosed by the six-helix barrel has a vestibular shape. This is represented in the form of a smoothed, surface-rendered volume of low (negative) density. The vestibule narrows to ~ 6.5 Å near the center of the bilayer where the location of the water-selective constriction is proposed. The scale bar represents 10 Å.

suggested pore location may house functionally important residues. The appropriate architecture and/or selectivity of the AQP1 channel may be contributed in part by some of these, channel-lining residues in addition to amino acid residues in the vicinity of the two conserved NPA motifs that have been shown (Jung *et al.*, 1994) to be important in water transport.

We may speculate on the nature and identities of the channel-lining residue in the absence of a complete atomic model. We note that the low-activation energy (4-5 kcal/mol) for osmotic water transport suggests that the pathway followed by water is relatively polar, similar to bulk water (Macey, 1984). In other words, the biophysical measurements suggest that a water molecule approaching the channel, and in its passage through the aqueous pore, thermodynamically behaves as if it were diffusing in bulk water. A hydrated pore (Welling *et al.*, 1996) within the hydrophobic core of the molecule, that is lined with polar or charged residues and sufficiently narrow for only water molecules to enter and exit by diffusive movements can adequately represent

such an environment. Residues expected to be located near the middle of the bilayer, where the narrow water selective pore is proposed, are shown in Figure 13(a), and a model for the azimuthal orientations of the helices was generated (Figure 13(b)). This was based on consensus secondary structure assignment, alignment of the sequences of aquaporin homolog, the criterion that conserved residues are likely to be involved in protein-protein contact and that polar and charged residues are either buried or tend to position near the edge of the bilayer. Such a model places polar and charged residues such as Glu17, Thr21, Thr22 and Ser28 in Helix 1, Ser59 and Thr62 in helix 2, Gln101 and Thr109 in helix 3, Glu142, Thr146 and Gln148 in helix 4, and Ser175 and His180 in helix 5 in the middle and the inside surface of the helix barrel. Some of these may line the pore and be structurally and/or chemically involved in channel function. Other conserved non-polar residues, especially glycine and proline residues (e.g. in helices 2, 3, 4, 5 and 6, Figure 13(a)) may be critical to the channel architecture, and thereby influence selectivity indirectly. These residues mentioned above are in addition to those belonging to the NPA box regions that have already been proposed (Froger *et al.*, 1998; Jung *et al.*, 1994) to be important for water transport.

Due to significant degree of sequence homology, it is likely that elements of the 3D structure, especially the fold of the polypeptide chain visualized for AQP1, is conserved amongst the aquaporins. However, chemical/structural changes localized at the entrance or exit of the narrowest part of the channel and/or distributed globally effecting the vestibular architecture (Figure 12) may be exploited to elicit the observed variability in the nature of the solute permeability. Undoubtedly, a concerted approach employing site-specific mutagenesis, dictated, for instance, by the proposed topology model and the candidate residues mentioned above, improved resolution of the density map to identify atomic details and biophysical measurements, should help provide further insight into how this ancient family of proteins play a fundamental role in cell homeostasis.

Conclusion

The unperturbed 3D structure of deglycosylated, human erythrocyte AQP1 has been determined at a nominal resolution of 4 Å parallel and ~7 Å perpendicular to the membrane bilayer by examination of frozen-hydrated 2D crystals preserved in ice. The densities for all of the six tilted transmembrane helices are characterized by protrusions, as expected for the near-atomic resolution data quality, and delineate the location of bulky side-chains. Sites of inter-helix contacts possibly mediated by side-chains are revealed that may contribute to the stabilization of the tertiary and quaternary structures. The density enclosed by the helix barrel,

which has been assigned to the polypeptide segments containing the NPA boxes, show improved definition, and is comparable in strength to that for a surrounding transmembrane helix. This density, which connects to the cytoplasmic and the extracellular faces of the bilayer, may harbor elements of secondary structure, such as short α -helices connected by short loops. The solvent-accessible region enclosed by the helix barrel has a vestibular architecture. The vestibule leads to a narrow ~6.5 Å diameter region near the middle of the bilayer where the water-selective pore is proposed to be located. Consistent with the observed inter-helix connections in a monomer, possible models for the threading of the AQP1 polypeptide chain were generated. Some of these models imply the presence of in-plane pseudo 2-fold symmetry relating the tandemly repeating motifs (Cheng *et al.*, 1997). A preferred model is deduced that agrees with the putative locations of a group of aromatic residues in the amino acid sequence and in the 3D density map.

Materials and Methods

2D crystallization

Highly ordered 2D crystals of deglycosylated AQP1 were prepared (Mitra *et al.*, 1995) by reconstitution of protein into DOPC bilayers. Outdated human erythrocytes (San Francisco and San Diego blood banks) were used to generate protein purified (van Hoek *et al.*, 1995) in the detergent *N*-octyl- β -D-glucopyranoside (OG; Anatrace, Maumee, Ohio). The concentrations of protein, lipid and detergent in the crystallization cocktail were 1.0 mg/ml, 0.28-0.33 mg/ml and 70-120 mM respectively in 20 mM $\text{NaH}_2\text{PO}_4/\text{Na}_2\text{HPO}_4$, 100 mM NaCl, 0.1 mM EDTA, 0.025% (w/v) NaN_3 , pH 7.2. When stored at 4°C, the reconstituted sample retained usable crystals for at least two months or up to eight months.

Preparation of frozen-hydrated ice-embedded specimens

Frozen-hydrated specimens were prepared in a cold room (4°C, ambient relative humidity 90%) using a plunge-freeze device (Dubochet *et al.*, 1988). Typically, reconstituted samples were allowed to settle for ~two minutes on a 300 mesh molybdenum grids overlaid with a flat, continuous carbon film that had been rendered hydrophilic by glow-discharging (60-90 seconds) in a saturated atmosphere (0.05 to 0.10 Torr) of amylamine. The grid was blotted with a preheated filter paper for 10-30 seconds and then plunged into liquid ethane slush to achieve vitrification. Specimens were also prepared by sandwiching crystals between two layers of carbon films. For this purpose, after allowing the suspension containing crystals to settle, excess sample was shaken off and then the grid was overlaid with another piece of carbon film. This was done by moving the grid, orienting with the specimen side-up through the carbon film floating on deionized water. Next, using a piece of preheated filter paper, the grid was blotted from the back for 15-20 seconds and the plunge freezing was carried out as usual.

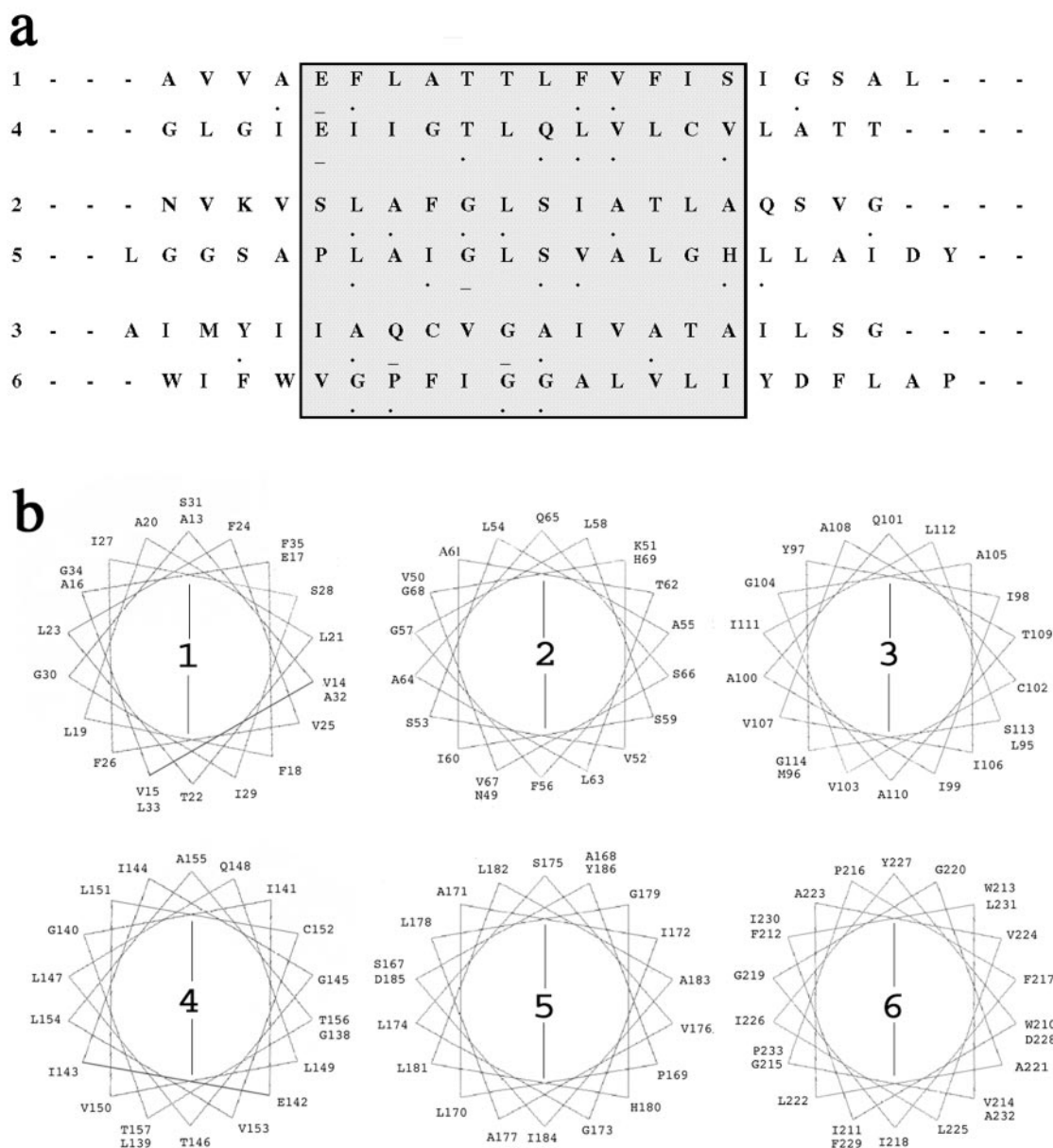


Figure 13. (a) Amino acid residues in the six transmembrane segments presented as three pairs of tandemly related stretches. The residues in the shaded box are expected to be near the middle of the bilayer and proximal to the water-selective pore. Amino acid residues with an underline and those with a dot below, respectively, represent residues that are very highly and highly conserved in mammalian aquaporins. (b) A helical wheel representation of the six putative trans-membrane segments of AQP1. For each segment the residues to the right of the vertical line are expected to be sequestered in the interior of the protein and/or line the protein-protein interaction surface.

Data Collection and processing

Ten of the selected images (four nominally untilted) and 16 of the selected electron diffraction patterns (one nominally untilted) in the final data set were collected on a Philips CM12 microscope operated at 100 kV using described protocols (Mitra & Stroud, 1990; Mitra *et al.*, 1995). For diffraction experiments, the nominal specimen to detector distance was chosen as 1.6 m, and the nominal imaging magnification was 48,000. The rest of the images and the diffraction patterns were collected using a Philips CM200FEG operated at 200 kV at a nominal

magnification of 50,000 or using a specimen to detector distance of 1.90 m. The extraction voltage for the field-emission gun was set at 3.95 kV, the gun lens was set in the cross-over mode, the smallest C1 condenser aperture (30 μm) was used to minimize the "holy-cross" effect and a 70 or 100 μm C2 condenser aperture was used. Images and electron diffraction patterns were recorded on Kodak SO-163 films, which were developed for 11 minutes in full-strength Kodak D-19 developer under nitrogen burst. Selected images and electron diffraction patterns were digitized on a Perkin Elmer PDS densitometer. Electron diffraction patterns were visually

assessed for quality, i.e. the presence of sharp spots to high resolution. The patterns were digitized using an aperture and step size of 10 μm so as to include data up to a resolution of 3.5 \AA or 3.0 \AA . Images were assessed for their quality on an optical diffractometer. The majority of the images from tilted crystals displayed strong non-isotropic fall-off perpendicular to the tilt axis due to non-flat carbon support film and specimen movement due to charging of the non-conducting vitreous ice. In all, only $\sim 3\%$ of the recorded images displaying sharp spots, minimum drift and astigmatism were chosen for processing. Selected areas of good images were digitized using an aperture and step size of 10 or 7 μm . For many of the highest tilt images, several small areas within a larger digitized region (8192 pixels) were pre-processed to select the best area. Such processed areas ranged in size from 2700 to 4608 voxels.

The digitized images and electron diffraction patterns were processed on a DEC/Alpha workstation following the protocol and the programs (MRC package) described by Henderson *et al.* (1990) and by Baldwin & Henderson (1984). In order to correct for lattice distortions (unbending), a reference area $\sim 10\%$ of the size of the digitized area and located in the most ordered part of an image, was excised from a noise-filtered image. This filtered image was created by including information within three reciprocal grid units around the position of all strong reflections up to a resolution of 10 or 7 \AA in the computed Fourier transform. Next, a cross-correlation calculation between the reference image and the original image was carried out. At most three passes of "unbending" that entailed simple interpolation of the cross-correlation peaks to predict the required correction was sufficient to minimize translational disorder. An area of the image that included cross-correlation peaks up to 50% of the maximum height was used to obtain the final set of phases and amplitudes. For nominally untilted images the defocus was determined using the program CTFREFINE using as a reference a set of merged amplitudes determined from nominally untilted electron diffraction patterns. Next the CTF correction to the phases were applied using the program CTFAPPLY. For tilted images, the phases were corrected for the effects of the "tilted" contrast transfer function (TTF) by using the programs TTREFINE and TTBOX starting with good approximations for the values of the defocus and astigmatism at the center of the image. The different images were brought to the same origin based on the phases of all reflections with $IQ \leq 7$ (in the nomenclature by Henderson *et al.*, 1986). First, all images upto 40° tilt were merged, followed by a refinement of the tilt angle and the orientation of the tilt axis of individual images carried out against the merged data set. Eight cycles of the refinement of the phase-origin and tilt parameters were carried out iteratively. Usually, a departure of no more than 2° in the tilt angle and 10° in the tilt axis were noted when compared to their starting values obtained using EMTILT. Next, the process was repeated by including images up to a tilt of 48° and then the highest tilt (up to 60°) images were added. The final merged data set was produced by including data from each image up to an in-plane "cut-off" resolution ($<12 \text{\AA}$). This cut-off was arbitrarily set as the resolution at which the phase residual for a given image, when compared to the full image data set, reached 50°. A lower threshold did not significantly alter the overall value of the phase residual in resolution shells.

Electron diffraction intensities of individual spots in a pattern were calculated using a peak profile-fitting algo-

ithm (PICKPROF) in the MRC package. A reflection was excluded if the average of the intensities of the Friedel pairs was less than their difference and greater than five times the standard deviation of such averages for all reflections in that pattern. The merging of the data involved scaling, application of anisotropic temperature factor, and tilt-axis and tilt-angle refinement. In this process, all data were equally weighted in order to avoid occasional underestimate of errors in measurements given as the difference between the Friedel-related pairs. These procedures were aimed at minimizing the difference between the calculated intensity of a given reflection with the merged and sync function-fitted lattice lines. Data from a given diffraction pattern truncated to a resolution where R_{Friedel} reached 20% (based on intensity) were included in the merging process. A lower threshold did not significantly alter the overall value of the R_{merge} in resolution shells.

The discreet values of merged phases and amplitudes for a lattice line were fit to a smooth function by a non-linear least-squares fitting according to the LATLINE program (Agard, 1983) using an estimate of 80 \AA for the vertical dimension of AQP1. The least-squares fitted lattice lines were sampled at z^* intervals of 0.01 \AA^{-1} to generate structure factors. The 3D density map was computed by inverse Fourier synthesis of only those structure factors for which the estimated standard deviation of sampled phase, calculated based on the local agreement along the lattice line (1/2 the error bar of sampled values in Figure 4) was $\leq 75^\circ$. The resolution of the 3D density map was estimated from the dimensions of a point spread function, which was created by setting the amplitudes of the reflections in the 3D data to the corresponding figure of merit and the phases to a constant value of 0° (Unger & Schertler, 1995).

Search and analysis of non-crystallographic symmetry in the 3D density map were performed by using a procedure that searched for density correlation within a monomer. This procedure avoided the problem associated with the partial overlap of correlation peaks due to the putative pseudo 2-fold and the crystallographic 2-fold when using the CCP4 program POLARFN in our previous analysis (Cheng *et al.*, 1997). For this purpose, a slab of density 21 \AA thick in the z -direction ($\rho_c(x',y',z')$) was excised from the density attributed to a monomer in the 3D map ($\rho_m(x,y,z)$) and was then rotated by 180° about the 'a' axis (x -axis of the 3D map). This rotated slab of density was compared to the full monomer density through a four-parameter search (x,y,z,ϕ) and the function $Q(x,y,z,\phi)$ was calculated, where:

$$Q(x,y,z,\phi) = \sqrt{\sum_{x',y',z'} [\rho_m(x+x', y+y', z+z') - \rho_c(x',y',z',\phi)]^2 / N}$$

Here, ρ_c now is the interpolated density after an in-plane rotation through ϕ , and N is the number of pixels compared. $Q(\phi)$, given as $\min[Q(x_0,y_0,z_0,\phi)]$ and $Q(z)$, given as $\min[Q(x_0,y_0,z_0,\phi_0)]$, are plotted against ϕ (Figure 8(a)) and z (Figure 8(b)), respectively.

Acknowledgments

We thank R. Henderson for advice regarding processing of tilted images. We are indebted to M. Pique for

generating the Figures depicting pertinent features of the 3D density map. The research was supported by a grant from the National Institutes of Health, in part by a grant from the National Science Foundation and a Grant-in-Aid from the American Heart Association and a special fellowship from the Cystic Fibrosis Research Foundation to A. K. M. G.R. was supported by a post-doctoral fellowship from the American Heart Association Western Affiliate and A.K.M. is an Established Investigator with the American Heart Association.

References

- Agard, D. A. (1983). A least-squares method for determining structure factors in three-dimensional tilted-view reconstructions. *J. Mol. Biol.* **167**, 849-852.
- Agre, P., Brown, D. & Nielsen, S. (1995). Aquaporin water channels: unanswered questions and unresolved controversies. *Curr. Opin. Cell Biol.* **7**, 472-483.
- Agre, P., Lee, M. D., Devidas, S. & Guggino, W. B. (1997). Aquaporins and ion conductance. *Science*, **275**, 1490-1492.
- Bai, L., Fushimi, K., Sasaki, S. & Marumo, F. (1996). Structure of aquaporin-2 vasopressin water channel. *J. Biol. Chem.* **271**, 5171-5176.
- Baldwin, J. & Henderson, R. (1984). Measurement and evaluation of electron diffraction patterns from two-dimensional crystals. *Ultramicroscopy*, **14**, 319-336.
- Bibi, E. (1998). The role of the ribosome-translocon complex in translation and assembly of polytopic membrane proteins. *Trend. Biol. Sci.* **23**, 51-55.
- Brink, J., Sherman, M. B., Berriman, J. & Chiu, W. (1998a). Evaluation of charging on macromolecules in electron cryomicroscopy. *Ultramicroscopy*, **72**, 41-52.
- Brink, J., Gross, H., Tittman, P., Sherman, M. B. & Chiu, W. (1998b). Reduction of charging in protein electron cryomicroscopy. *J. Microsc.* **191**, 67-73.
- Carfi, A., Pares, S., Duee, E., Galleni, M., Duez, C., Frere, J. M. & Dideberg, O. (1995). The 3D structure of a zinc metallo-beta-lactamase from *Bacillus cereus* reveals a new type of protein fold. *EMBO J.* **14**, 4914-4921.
- Ceska, T. A. & Henderson, R. (1990). Analysis of high-resolution electron diffraction patterns from purple membrane labelled with heavy-atoms. *J. Mol. Biol.* **213**, 539-560.
- Cheng, A., van Hoek, A. N., Yeager, M., Verkman, A. S. & Mitra, A. K. (1997). Three-dimensional organization of a human water channel. *Nature*, **387**, 627-630.
- Chothia, C., Levitt, M. & Richardson, D. (1981). Helix to helix packing in proteins. *J. Mol. Biol.* **145**, 215-250.
- Deen, P. M., Verdijk, M. A., Knoers, N. V., Wieringa, B., Monnens, L. A., van Os, C. H. & van Oost, B. A. (1994). Requirement of human renal water channel aquaporin-2 for vasopressin-dependent concentration of urine. *Science*, **264**, 92-95.
- Denker, B. M., Smith, B. L., Kuhajda, F. P. & Agre, P. (1988). Identification, purification, and partial characterization of a novel M_r 28,000 integral membrane protein from erythrocytes and renal tubules. *J. Biol. Chem.* **263**, 15634-15642.
- Dubochet, J., Adrian, M., Chang, J. J., Homo, J. C., Lepault, J., McDowell, A. W. & Schultz, P. (1988). Cryo-electron microscopy of vitrified specimens. *Quart. Rev. Biophys.* **21**, 129-228.
- Engel, A., Walz, T. & Agre, P. (1994). The aquaporin family of membrane water channels. *Curr. Opin. Struct. Biol.* **4**, 545-553.
- Froger, A., Tallur, B., Thomas, D. & Delamarche, C. (1998). Prediction of functional residues in water channels and related proteins. *Protein Sci.* **7**, 1458-1468.
- Gorin, M. B., Yancey, S. B., Cline, J., Revel, J. P. & Horwitz, J. (1984). The major intrinsic protein (MIP) of the bovine lens fiber membrane: characterization and structure based on cDNA cloning. *Cell*, **39**, 49-59.
- Grigorieff, N., Ceska, T. A., Downing, K. H., Baldwin, J. M. & Henderson, R. (1996). Electron-crystallographic refinement of the structure of bacteriorhodopsin. *J. Mol. Biol.* **259**, 393-421.
- Henderson, R., Baldwin, J. M., Downing, K. H., Lepault, J. & Zemlin, F. (1986). Structure of purple membrane from halobacterium halobium: recording, measurement and evaluation of electron micrographs at 3.5 Å resolution. *Ultramicroscopy*, **19**, 147-178.
- Henderson, R., Baldwin, J. M., Ceska, T. A., Zemlin, F., Beckmann, E. & Downing, K. H. (1990). Model for the structure of bacteriorhodopsin based on high-resolution electron cryo-microscopy. *J. Mol. Biol.* **213**, 899-929.
- Heymann, J. B. & Engel, A. (2000). Structural clues in the sequences of the aquaporins. *J. Mol. Biol.* **295**, 1039-1053.
- Heymann, J. B., Agre, P. & Engel, A. (1998). Progress on structure and function of aquaporin 1. *J. Struct. Biol.* **121**, 191-206.
- Iwata, S., Ostermeier, C., Ludwig, B. & Michel, H. (1995). Structure at 2.8 Å resolution of cytochrome c oxidase from *Paracoccus denitrificans*. *Nature*, **376**, 660-669.
- Jap, B. K. & Li, H. (1995). Structure of the osmo-regulated H₂O-channel, AQP-CHIP, in projection at 3.5 Å resolution. *J. Mol. Biol.* **251**, 413-420.
- Jung, J. S., Preston, G. M., Smith, B. L., Guggino, W. B. & Agre, P. (1994). Molecular structure of the water channel through aquaporin CHIP. The hourglass model. *J. Biol. Chem.* **269**, 14648-14654.
- Kimura, Y., Vassilyev, D. G., Miyazawa, A., Kidera, A., Matsushima, M., Mitsuoka, K., Murata, K., Hirai, T. & Fujiyoshi, Y. (1997). Surface of bacteriorhodopsin revealed by high-resolution electron crystallography. *Nature*, **389**, 206-211.
- Kühlbrandt, W. & Wang, D. N. (1991). Three-dimensional structure of plant light-harvesting complex II by electron crystallography. *Nature*, **350**, 130-134.
- Kühlbrandt, W., Wang, D. N. & Fujiyoshi, Y. (1994). Atomic model of plant light-harvesting complex by electron crystallography. *Nature*, **367**, 614-621.
- Li, H., Lee, S. & Jap, B. K. (1997). Molecular design of aquaporin-1 water channel as revealed by electron crystallography. *Nature Struct. Biol.* **4**, 263-265.
- Luecke, H., Schobert, B., Richter, H. T., Cartailler, J. P. & Lanyi, J. K. (1999). Structure of bacteriorhodopsin at 1.55 Å resolution. *J. Mol. Biol.* **291**, 899-911.
- Luger, K., Mader, A. W., Richmond, R. K., Sargent, D. F. & Richmond, T. J. (1997). Crystal structure of the nucleosome core particle at 2.8 Å resolution. *Nature*, **389**, 251-260.
- Macey, R. I. (1984). Transport of water and urea in red blood cells. *Am. J. Physiol.* **246**(3 Pt 1), C195-203.
- Mitra, A. K. & Stroud, R. M. (1990). High sensitivity electron diffraction analysis. A study of divalent

- cation binding to purple membrane. *Biophys. J.* **57**, 301-311.
- Mitra, A. K., Yeager, M., van Hoek, A. N., Wiener, M. C. & Verkman, A. S. (1994). Projection structure of the CHIP28 water channel in lipid bilayer membranes at 12-Å resolution. *Biochemistry*, **33**, 12735-12740.
- Mitra, A. K., van Hoek, A. N., Wiener, M. C., Verkman, A. S. & Yeager, M. (1995). The CHIP28 water channel visualized in ice by electron crystallography [letter]. *Nature Struct. Biol.* **2**, 726-729.
- Mitra, A. K. (2000). Three-dimensional organization of aquaporin water channel: what can structure tell us about function? *Vitamins and Hormones*, in the press.
- Mitsuoka, K., Murata, K., Walz, T., Hirai, T., Agre, P., Heymann, J. B., Engel, A. & Fujiyoshi, Y. (1999). The structure of aquaporin-1 at 4.5-Å resolution reveals short α -helices in the center of the monomer. *J. Struct. Biol.* **128**, 34-43.
- Miyazawa, A., Fujiyoshi, Y., Stowell, M. & Unwin, N. (1999). Nicotinic acetylcholine receptor at 4.6 Å resolution: transverse tunnels in the channel wall. *J. Mol. Biol.* **288**, 765-786.
- Nakhoul, N. L., Davis, B. A., Romero, M. F. & Boron, W. F. (1998). Effect of expressing the water channel aquaporin-1 on the CO₂ permeability of *Xenopus* oocytes [see comments]. *Am. J. Physiol.* **274**(2 Pt 1), C543-C548.
- Nielsen, S., Smith, B. L., Christensen, E. I., Knepper, M. A. & Agre, P. (1993). CHIP28 water channels are localized in constitutively water-permeable segments of the nephron. *J. Cell. Biol.* **120**, 371-383.
- Nogales, E., Wolf, S. G. & Downing, K. H. (1998). Structure of the alpha beta tubulin dimer by electron crystallography. *Nature*, **391**, 1999-2003.
- Pao, G. M., Wu, L.-F., Johnson, K. D., Höfte, H., Chrispeels, M. J., Sweet, G., Sandal, N. N. & Saier, M. H., Jr (1991). Evolution of the MIP family of integral membrane transport proteins. *Mol. Microbiol.* **5**, 33-37.
- Prasad, G. V., Coury, L. A., Finn, F. & Zeidel, M. L. (1998). Reconstituted aquaporin 1 water channels transport CO₂ across membranes. *J. Biol. Chem.* **273**, 33123-33126.
- Preston, G. M. & Agre, P. (1991). Isolation of the cDNA for erythrocyte integral membrane protein of 28 kilodaltons: member of an ancient channel family. *Proc. Natl Acad. Sci. USA*, **88**, 11110-11114.
- Preston, G. M., Jung, J. S., Guggino, W. B. & Agre, P. (1993). The mercury-sensitive residue at cysteine 189 in the CHIP28 water channel. *J. Biol. Chem.* **268**, 17-20.
- Preston, G. M., Smith, B. L., Zeidel, M. L., Moulds, J. J. & Agre, P. (1994). Mutations in aquaporin-1 in phenotypically normal humans without functional CHIP water channels. *Science*, **265**, 1585-1587.
- Rader, R. S. & Lamvik, M. K. (1992). High-conductivity amorphous TiSi substrates for low-temperature electron microscopy. *J. Microsc.* **168**, 71-77.
- Ren, G., Cheng, A., Melnyk, P. & Mitra, A. K. (2000). Polymorphism in the packing of aquaporin-1 tetramers in 2D crystals. *J. Struct. Biol.* **130**, 45-53.
- Shi, L. B., Skach, W. R. & Verkman, A. S. (1994). Functional independence of monomeric CHIP28 water channels revealed by expression of wild-type mutant heterodimers. *J. Biol. Chem.* **269**, 10417-10422.
- Smith, B. L. & Agre, P. (1991). Erythrocyte Mr 28,000 transmembrane protein exists as a multisubunit oligomer similar to channel proteins. *J. Biol. Chem.* **266**, 6407-6415.
- Unger, V. M. & Schertler, G. F. X. (1995). Low resolution structure of bovine rhodopsin determined by electron cryo-microscopy. *Biophys. J.* **68**, 1776-1786.
- Upton, C., Faulheber, T., Jr., Kamins, D., Laidlaw, D., Schlegel, D., Vroom, J., Gurwitz, R. & Van Dam, A. (1989). The application visualization system: a computational environment for scientific visualization. *Comput. Graph. Appl.* **9**, 30-42.
- van Hoek, A. N., Hom, M. L., Luthjens, L. H., de Jong, M. D., Dempster, J. A. & van Os, C. H. (1991). Functional unit of 30 kDa for proximal tubule water channels as revealed by radiation inactivation. *J. Biol. Chem.* **266**, 16633-16635.
- van Hoek, A. N., Wiener, M. C., Verbavatz, J. M., Brown, D., Lipniunas, P. H., Townsend, R. R. & Verkman, A. S. (1995). Purification and structure-function analysis of native, PNGase F-treated, and endo- β -galactosidase-treated CHIP28 water channels. *Biochemistry*, **34**, 2212-2219.
- Varughese, K. I., Skinner, M. M., Whiteley, J. M. & Matthews, D. A. (1992). Crystal structure of rat liver dihydropteridine reductase. *Proc. Natl Acad. Sci. USA*, **89**, 6080-6084.
- Verbavatz, J. M., Brown, D., Sabolic, I., Valenti, G., Ausiello, D. A., Van Hoek, A. N., Ma, T. & Verkman, A. S. (1993). Tetrameric assembly of CHIP28 water channels in liposomes and cell membranes: a freeze-fracture study. *J. Cell Biol.* **123**, 605-618.
- Verkman, A. S. & Mitra, A. K. (2000). Structure and function of aquaporin water channels. *Am. J. Physiol.* **278**, F13-F28.
- Verkman, A. S., van Hoek, A. N., Ma, T., Frigeri, A., Skach, W. R., Mitra, A., Tamarappoo, B. K. & Farinas, J. (1996). Water transport across mammalian cell membranes. *Am. J. Physiol.* **270**, C12-30.
- Walz, T., Typke, D., Smith, B. L., Agre, P. & Engel, A. (1995). Projection map of aquaporin-1 determined by electron crystallography [letter]. *Nature Struct Biol.* **2**, 730-732.
- Walz, T., Tittmann, P., Fuchs, K. H., Muller, D. J., Smith, B. L., Agre, P., Gross, H. & Engel, A. (1996). Surface topographies at subnanometer-resolution reveal asymmetry and sidedness of aquaporin-1. *J. Mol. Biol.* **264**, 907-918.
- Walz, T., Hirai, T., Murata, K., Heymann, J. B., Mitsuoka, K., Fujiyoshi, Y., Smith, B. L., Agre, P. & Engel, A. (1997). The three-dimensional structure of aquaporin-1. *Nature*, **387**, 624-627.
- Welling, D. J., Welling, P. A. & Welling, L. W. (1996). Filled pore approximation: a theoretical framework for solute-solvent coupling in narrow water channels. *Am. J. Physiol.* **270**, C1246-1254.
- Wistow, G. J., Pisano, M. M. & Chepelinsky, A. B. (1991). Tandem sequence repeats in transmembrane channel proteins. *Trends Biochem. Sci.* **16**, 170-171.
- Yang, B., Fukuda, N., van Hoek, A., Matthay, M. A., Ma, T. & Verkman, A. S. (2000). Carbon dioxide permeability of aquaporin-1 measured in erythrocytes and lung of aquaporin-1 null mice and reconstituted proteoliposomes. *J. Biol. Chem.* **275**, 2686-2692.
- Yool, A. J., Stamer, W. D. & Regan, J. W. (1996). Forskolin stimulation of water and cation permeability in aquaporin 1 water channels. *Science*, **273**, 1216-1218.

- Zeidel, M. L., Ambudkar, S. V., Smith, B. L. & Agre, P. (1992). Reconstitution of functional water channels in liposomes containing purified red cell CHIP28 protein. *Biochemistry*, **25**, 7436-7440.
- Zeidel, M. L., Nielsen, S., Smith, B. L., Ambudkar, S. V., Maunsbach, A. B. & Agre, P. (1994). Ultrastructure, pharmacologic inhibition, and transport selectivity of aquaporin channel-forming integral protein in proteoliposomes. *Biochemistry*, **33**, 1606-1615.
- Zhang, R., van Hoek, A. N., Biwersi, J. & Verkman, A. S. (1993). A point mutation at cysteine 189 blocks the water permeability of rat kidney water channel CHIP28k. *Biochemistry*, **32**, 2938-2941.

Edited by W. Baumeister

(Received 3 May 2000; received in revised form 6 June 2000; accepted 6 June 2000)